A new experimental method for characterizing boiling regimes of water in vertical milli-channels

Guillaume Henry, Alexandra Pere-Gigante, Jacopo Seiwert, Solène Valentin, Marc Wagner, Émilien Girot, François Mendy, Jean-Marc Jean-Marc.Commenge@univ-Lorraine.Fr Commenge

A new experimental method for characterizing boiling regimes of water in vertical milli-channels

Guillaume HENRY[a,*], Alexandra PERE-GIGANTE[a], Jacopo SEIWERT[b], Solène VALENTIN[b], Marc WAGNER[b], Émilien GIROT[a], François MENDY[a], Jean-Marc COMMENGE[a]

[a] Université de Lorraine, CNRS, Laboratoire Réactions et Génie des Procédés, UMR 7274, Nancy, F-54000
[b] Air Liquide, Centre de Recherche Paris-Saclay, 1 chemin de la Porte des Loges, Les Loges-en-Josas, BP 126, 78354 Jouy-en-Josas, France
*Corresponding author: guillaume.henry@univ-lorraine.fr

Address: 1 rue Grandville, BP 20451, F-54001 NANCY Cedex

Abstract

Over the past few decades, high-performance heat-transfer devices have been studied for numerous applications. Boiling flow in such confined spaces induces high-frequency flow instabilities that directly influence the heat-transfer performances. A small-scale water vaporizer with 10 millimeter-sized channels is experimentally studied over a wide range of vapor quality (0.05 – 1). The peculiarity of the setup is a transparent window that allows for high speed imaging of the boiling flow up to 5 bars. This work focuses on a post-processing method based on spatio-temporal diagrams. Hydrodynamics of the boiling flow can be observed on the diagrams enabling to understand the boiling mechanisms and the flow regimes inside the channels. Four regimes are observed, namely bubbly, slug, churn and annular flow. Diagrams are also used to estimate the local mean void fraction over time in channels, the local vapor quality, the slip ratio and a flow-regime map. For qualities under 10%, the bubbly flow is predominant in channel. For higher qualities, if the specific mass flow rate of water is below 37 kg/s/m², only the slug flow and the annular flow are observed, whereas the churn flow is also observed for larger flow rates.

Keywords: boiling flow, flow map, milli-channels, high-speed visualization, quality, heat transfer.

1. Introduction

Heat exchangers with millimeter-sized channels have raised a significant interest in the field of chemical engineering over the last few decades and for numerous industrial applications. Reference books, Stankiewicz and Moulijn [1], Dietrich [2] and Hessel et al. [3], develop the concept of process intensification by presenting the existing equipment and methods used. In particular, the main benefits of using microstructures is their high compactness and their high volume/surface ratio, which enables a better control of operating parameters such as fluid temperature or flow mixing. Meanwhile, the ever-growing interest for hydrogen as an alternative for cleaner mobility requires new process designs for its production (Surla [4]). Indeed, the main part of the hydrogen is currently produced by Steam Methane Reforming (SMR) processes and close to refinery plants (Giroudière et Le Gall [5]). Since hydrogen transport suffers from numerous hazards (explosiveness, leakages, etc.), a decentralized production is required for the deployment of this new vector of energy.

Some studies have been performed on the intensification of the reformer; Frauhammer et al. [6] studied the applicability of counter-current reformer with capillarity tubes. More recently, Bhat and Sadhukhan [7] presented in their review various ways to intensify the reforming process, e.g. by improving catalyst efficiency or using membranes. Although there exist technical solutions to intensify the reforming reactor, all the other pieces of equipment (heat-exchanger, separator, etc.) operating in the process have also to be considered for intensification.

This study focuses on the vaporizer of the SMR process called the Waste Heat Boiler (WHB), which valorizes the remaining heat of hot gases outgoing the heat-exchanger reactor as steam (required for the reforming reaction). Intensification of industrial WHB, usually designed as shell-and-tubes heat exchangers, can be performed using milli-channels.

Boiling flow in milli- or micro-structures has led to numerous publications during the past fifty years. Numerous modern applications, such as microchips cooling, require an efficient heat transfer to operate properly. In most studies, the fluid is a typical refrigerant such as HFE7100 for Solotych et al. [8] or R134a for Sempertegui-Tapia et al. [9] because of its low boiling temperature and its compatibility with electronic devices. However, recently water raised a new interest since it is a non-pollutant fluid with a high latent heat of vaporization (often ten times larger than freons) enabling a better heat recovery at a later stage.

One key parameter of boiling flow heat transfer is the two-phase heat-transfer coefficient, which indicates the performance of a micro/milli-heat exchanger. Some authors, for instance Lazarek and Black [10], Kew and Cornwell [11] or Pamitran et al.[12], worked on a predictive general correlation of this coefficient for various operating conditions and fluids. The recent review of Cheng and Xia [13] highlights the fact that these correlations are still not accurate for all experimental data available in the literature. Furthermore, the same operating conditions can lead to different values of heat-transfer coefficient, which confirms that boiling phenomena are complex to predict correctly. In addition, conclusions of a specific review by Fang et al. [14] highlight that there is no accurate correlation to predict subcooled flow boiling heat transfer applied to water.

The identification of the different two-phase flow regimes in a milli-channel is crucial for the understanding of heat transfer between the fluid and the walls of the channel. Focusing on the case of boiling water in channels, Yin et al. [15] studied the effect of the Boiling number, Bo, for large aspect ratio microchannel on boiling flow regimes. They observed the flow regime

transitions through the following patterns with increasing Bo: discrete bubble flow, confined bubble flow, sweeping flow, churn flow and wispy flow when Critical Heat Flux is reached. Lu et al. [16] also described for water the isolated bubbly flow, the slug flow, the churn flow and the annular flow in conventional vertical channels. However, for vertical mini-channels, they reported that the effect of surface tension and the confinement force the bubbles to quickly coalesce leading to a predominant slug flow regime.

It is commonly admitted that boiling flow heat transfer can be related to two main heat-transfer mechanisms: nucleate boiling and convective boiling heat transfer. Both of these mechanisms encompass several flow regimes. According to Kim and Mudawar [17], nucleate boiling mechanism gathers dominant bubbly and slug flow regime whereas the convective boiling mechanism presents a dominant annular flow regime. Furthermore, Kim and Mudawar [17] present three scenarios where the value of the heat-transfer coefficient is directly related to flow regimes inside the micro/milli-structure. In numerous predictive heat-transfer models, e.g. Chen's correlation [18] or most recently the Chen derived correlation published by Yan et al. [19], the two mechanisms are taken into account and are weighted as a function of the vapor quality.

According to Kandlikar [20] and Thome [21], the effects of capillarity on flow regimes inside the channel only occur at a micro-scale. The Kumar et al. [22] review highlights an unclear threshold to classify geometries in the micro/milli/macro-scale. Some thresholds are based on geometry parameters such as the hydraulic diameter whereas others rely on dimensionless numbers such as the Boiling number. Kumar et al. [22] suggest a threshold between micro- and macro-scale at a hydraulic diameter of 1 mm. According to this limit, the 2 mm semi-circular channels studied (D_h = 1.22 mm) in this paper are considered macro-channels. Therefore, flow regimes similar to those presented in details by Chen [23] are expected, namely bubbly, slug, churn and annular flow. Nevertheless, in order to avoid any confusion

about this unclear threshold, it has been decided to qualify the studied channels according to their dimension and not their type, e.g. milli-channels.

High-frequency films are a common practice for the identification of boiling flow regime in milli- or microstructures since observed phenomena last less than one second. Flow regime observations on a single channel, in various references in the literature, are presented through a sequence of channel pictures with a specific time step. Steinke and Kandlikar [24] used this method to present flow reversal and micro-channel dry-out flow of a water boiling flow in a single vertical channel. More recently, Yin et al. [15] also used it to present the effect of the Boiling number on the flow regime observed. The sweeping, the churn and wispy flow are also described. If this common method enables to highlight a specific phenomenon in the channels, it is not well adapted to describe all the boiling events over time and the related instabilities. The description of all the phenomena can become a tedious task if a consequent number of pictures has to be temporally spotted, extracted and presented.

In this work, an original post-treatment method of high-speed movies of a water boiling flow in vertical semi-circular channels is developed. The result of this method is called spatio-temporal diagrams. It enables the spotting and the understanding of localized hydrodynamics that occur in the channels and flow boiling patterns and regimes can be identified. A quantitative approach of the spatio-temporal diagram is applied to assess the local quality in channels in order to draw a flow-regime map. The thermal performance of a small-scale water vaporizer measured experimentally under various operating conditions is used to validate this approach. In addition, the global vapor quality produced by the vaporizer is also discussed.

2. Material

2.1. Experimental set-up

For this work, a dedicated test bench was built to operate intensified industrial waste heat boiler at laboratory scale; its Process & Instrumentation Diagram (P&ID) is presented in *Figure 1*. The spatial organization of the test bench is presented in *Figure 2*. Three different loops of fluids are required: a hot utility loop to provide heat, another one for the process fluid (water) being preheated and vaporized and the last one to condensate the produced vapor. The hot loop uses a silicon oil flow as the heat-transfer fluid. Instead of using a classical electrical resistance, a silicon oil as heating source has been preferred in order to limit the wall temperature on the water side. Indeed, an electrical resistance cannot reproduce the thermal exchange between two fluids since its temperature and its heat flux cannot be controlled separately.

A JULABO SE-6 temperature-controlled bath (20 – 300 °C; 3 kW; n° 1) heats Julabo Thermal HS silicon oil. The hot oil is pumped by a MAAG Refinex 22/22 gear pump (1 – 10 L/min; n° 2) and its flow rate is measured by a YOKOGAWA Rotamass Nano Coriolis flowmeter (0 – 950 kg/h; n° 3). The discharge pressure of the pump is measured by a YOKOGAWA absolute pressure sensor (0 - 20 bars; n°4) to ensure safe operation of the pump.

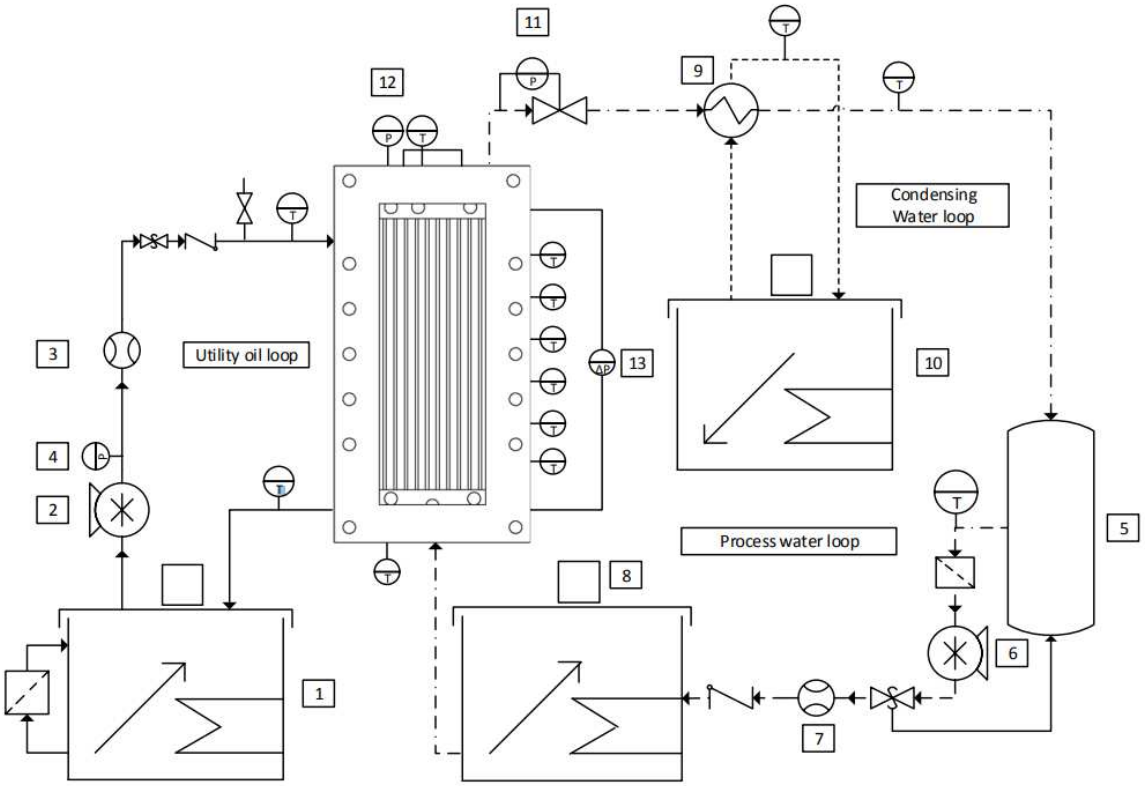

Figure 1: Process & Instrumentation Diagram of the test bench (1: oil bath; 2: oil pump; 3: oil flowmeter; 4: oil pressure sensor; 5: water tank; 6: process water pump; 7: water flowmeter; 8: process water preheater; 9: condenser heat-exchanger; 10: cooler; 11: pressure controller; 12: absolute pressure sensor; 13: differential pressure sensor).

The process fluid, demineralized water, is stored in a tank at room temperature (n° 5). The fluid is pumped by a HNP Mikrosystem mzr-7205 gear pump (0.048 – 248 mL/min; n° 6) and the flow rate is measured by a BRONKHORST mini CORI-FLOW Coriolis flowmeter (0.4 – 20 kg/h; n° 7). Before entering the test section, the flow is preheated through helical spires by silicon oil in a JULABO ME-6 temperature-controlled bath (20 – 200 °C; 2 kW; n° 8). At the test section outlet, the two-phase flow is condensed in a plate heat exchanger (n° 9) cooled by cold water provided by a JULABO FL-1201 cooler (-20 – 40 °C; 1.2 kW; n° 10). The pressure inside the test section is regulated by a QBS Equilibar discharge pressure controller (1 – 5 bars; n° 11).

Temperatures are measured at various locations in the test bench by 1/10 DIN PT 100 sensors. In the hot oil fluid loop, the sensors are located at the inlet and outlet of the test section in order to estimate the heat flux provided by the oil flow. In the process fluid loop, the temperature is measured in the test section, and at the outlet of the condenser to control its cooling efficiency.

The test bench operates the test section called vaporizer, which is a milli-structured plate heat exchanger manufactured in house. The vaporizer (130 mm x 250 mm x 50 mm), presented in *Figure 3*, is composed of four different parts: a borosilicate glass and three stainless steel engraved plates. Both water and oil flows enter the vaporizer through the multi-tasks block: the water just flows through the block via chambers whereas the oil flow is contained in the rectangular cross-section channel (2.5 mm x 9 mm) in the middle of the block. More precisely, the water enters at the bottom of the multi-task block inside the distribution chamber, then the water flow is vaporized along ten vertical semi-circular cross-section channels (diameter 2 mm) mechanically engraved with a total length of 180 mm. Finally, the two-phase water flow is gathered in the collection chamber located at the top of the plate and the multi-task block before leaving the vaporizer. Hydrodynamics in the channels can be observed through the borosilicate window (11 mm thick) maintained by the lid. This vaporizer was designed to operate a boiling flow under a maximum pressure of five bars. In order to ensure the insulation of the vaporizer, a custom insulating coat, made from MATELIS 500 material (glass fibers fabric, thickness 6 mm), encapsulates the test section.

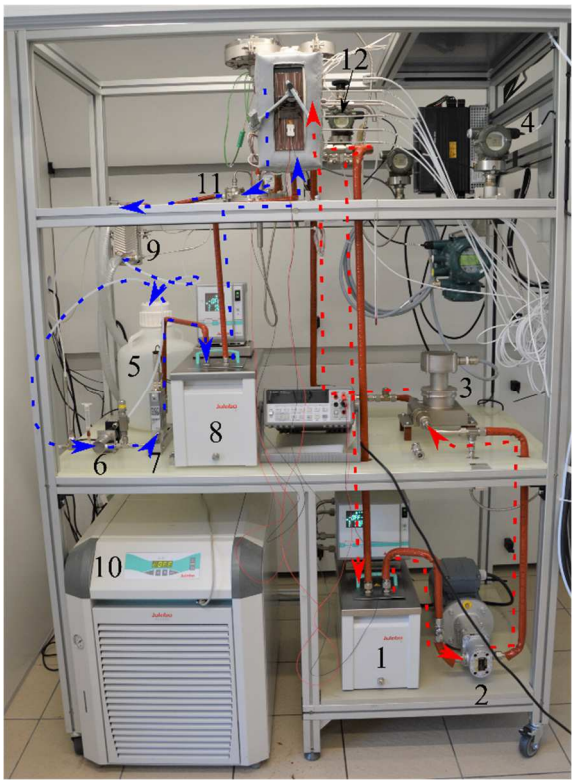

Figure 2: Spatial organization of the test bench (numbers refer to caption of Figure 1)

Some data are directly measured in the test section, namely the temperature with PT100 sensors in both chambers, the pressure in the collection chamber by a YOKOGAWA absolute pressure sensor (0 - 20 bars, n° 12) and the differential pressure along channels by a YOKOGAWA differential pressure sensor (0 – 5 bars, n° 13). The temperature at the center of the dividing wall between the hot oil and the boiling water is measured along the milli-structured plate by PT100 sensors placed in dedicated holes (*Figure 3*). In addition, heat losses are measured during specific experiments with two heat flux meters FHF02 from HUKSEFLUX, positioned on the borosilicate window and on the back of the vaporizer, on the insulating coat. The heat flux meter on the window is visible in *Figure 2*, it is maintained with a metallic clamp. The thermal contact between the patch and the surface is ensured by a thermal conductor sheet.

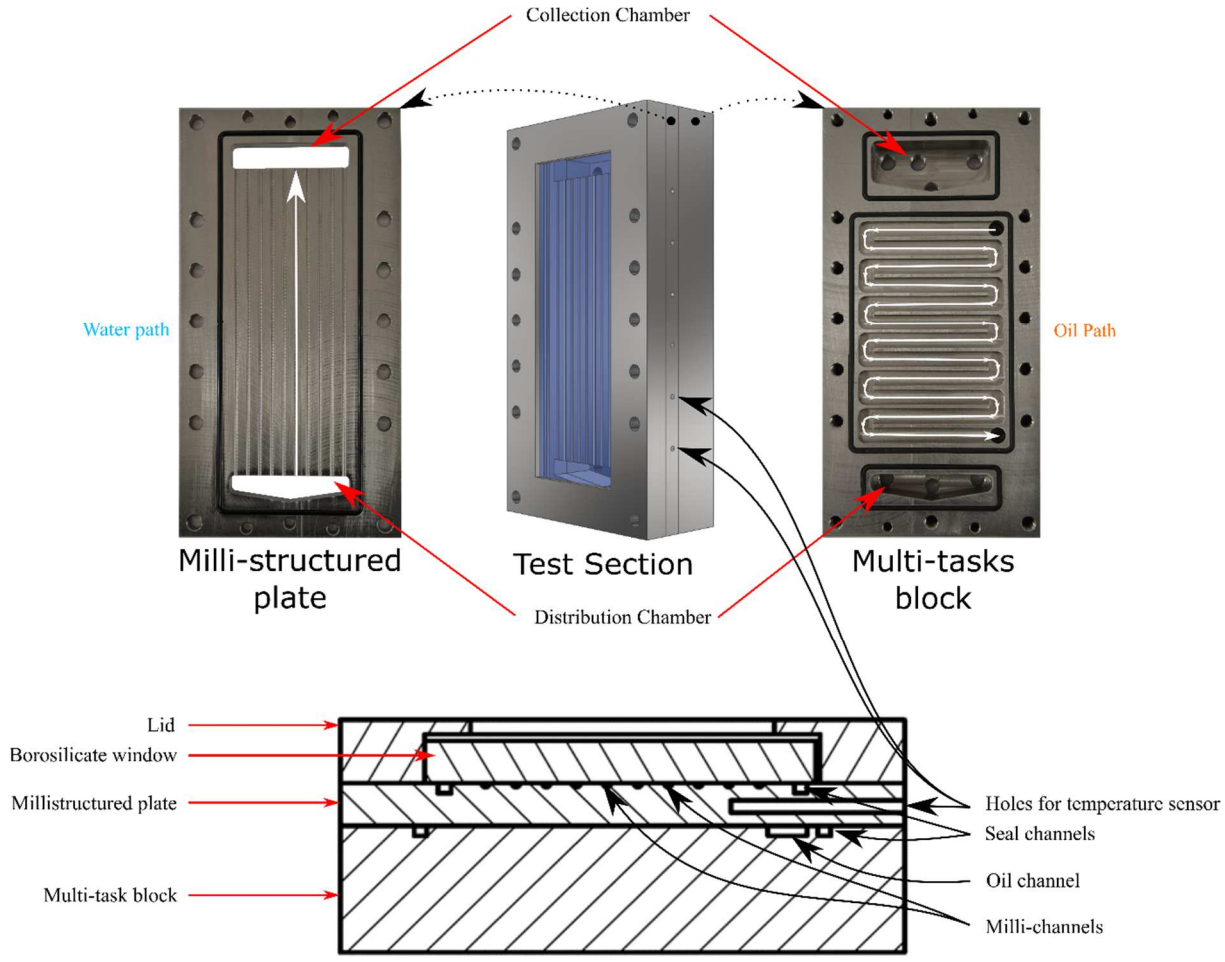

Figure 3: Detailed view of the test section (vaporizer): assembled (middle), milli-structured plate (left), multi-task block (right) and horizontal cross-sectional view of the vaporizer (bottom).

2.2. Experimental operating conditions

The possible ranges of the operating parameters are summarized in *Table 1*.

Operating parameter	***Range***	***Unit***
Hot oil flow rate	180 (0.05)	kg/h (kg/s)
Water flow rate	0.3 – 6 ($8.3\ 10^{-8}$ – $1.67\ 10^{-6}$)	L/h (m^3/s)
Corresponding to a specific water flow rate	5 – 53	kg/m² s

Oil temperature	130 – 180	°C
Water pre-heating temperature	30 – 130	°C
Pressure	1 (10^5)	Bar (Pa)

Table 1: Experimental operating parameters ranges.

In this work, only experiments performed at atmospheric pressure are presented. Moreover, the oil flow rate is fixed at 180 kg/h since specific experiments highlighted the small influence of the oil flow rate on the vapor quality produced (±12% over an oil flow rate range from 75 to 180kg/h). These experiments are not presented here for the sake of concision.

2.3. High-speed camera

Hydrodynamics of the flow in the channels is recorded by a high-frequency MIKROTRON EoSense mini 2© camera (up to 523 frames per second). The test section is illuminated by three light sources, covered by a layer of tracing paper for more homogeneous illumination. Since the internal data storage of the camera is limited, the shooting duration is influenced by two main parameters: the framerate of capture and the size of the Region Of Interest (ROI). This size impacts the size (in bytes) of each frame captured, therefore, it impacts the global number of frames that can be stored in the camera memory. Here, we chose a fixed framerate of 420 fps for an acquisition time between 5 and 10 seconds, depending on the size of the ROI.

2.4. Experimental procedure

The first step of the experimental procedure consists in setting all operating parameters, then all the measurable data on the test bench are picked up at steady state when the temperatures of the test section are stabilized (which takes about one hour and a half for the first experiment starting at ambient temperature and about half an hour after a change of one of the operating parameters for each further experiment). The picked-up data are: the inlet and outlet

temperatures of both oil and water flows, the temperatures of the milli-structured plate, the vaporizer pressure, and the mass flow rates of water and oil. A film of the boiling water is then recorded.

3. Experimental methods and data treatment for analysis of flow regimes

3.1. Spatio-Temporal Diagrams

Stacking images coming from high-speed movies is a simple and an easy method to present the evolution of the boiling flow inside a channel. However, it can only show a short extract of the movies for sake of clarity. In this work, a new film post processing based on the creation of Spatio-Temporal Diagrams has been developed in order to enlarge duration of the high-speed movie presented. It is elementarily described in *Figure 4*. A simplified film is studied in this example to allow for a better understanding of the method.

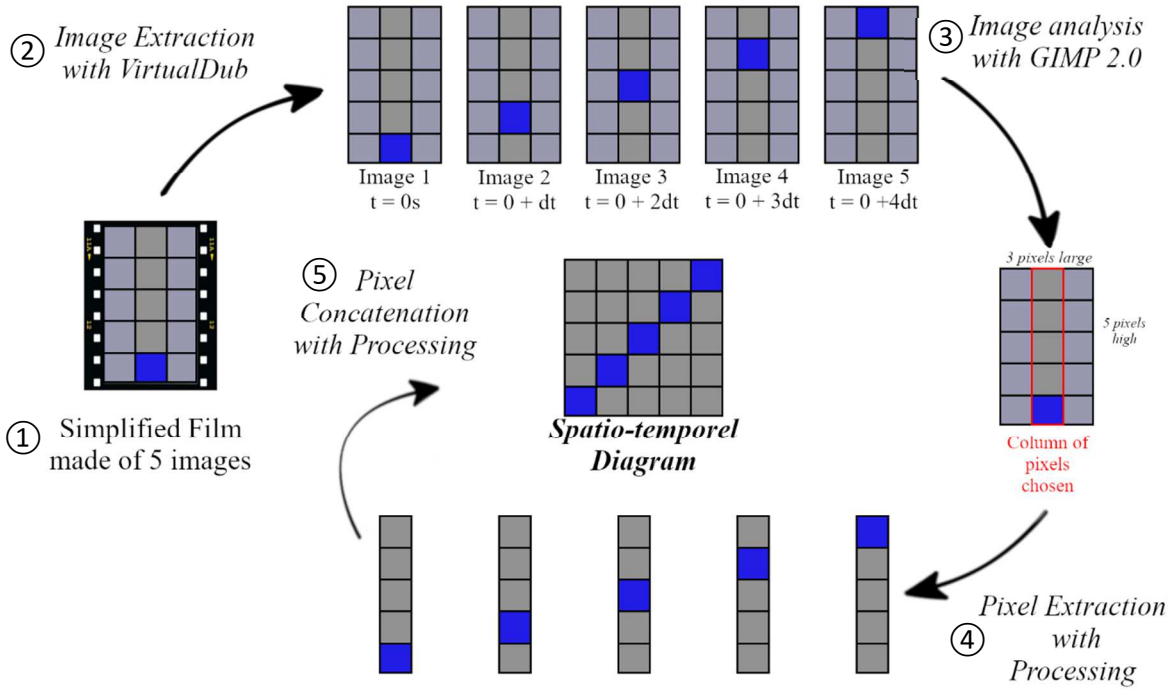

Figure 4: Method used to create spatio-temporal diagrams applied on a simple case.

A film is composed of many images scrolling at a chosen framerate. The software VirtualDub (step 2) is used to extract the image sequence from the film, composed by $\boldsymbol{k}$ images (k = 5 for the example). Each extracted image has the same dimensions corresponding to a matrix of ($\boldsymbol{m}$ *lines* x $\boldsymbol{n}$ *columns*) pixels (m = 5 and n = 3 in the example). In this study, since the camera is fixed on a tripod, the recorded film represents a static view of channels engraved in the milli-structured plate. It means that channels in the plate can be linked to columns of pixels in the images composing the film. To do that (step 3), the software GNU Image Manipulation Program (GIMP 2.0) is used to spot columns of pixels corresponding to channels. The average width of each channel on pictures is about 20 pixels. Among these 20 columns, only one column is chosen for post-treatment, it is generally extracted in the middle of the channel where a better exposure is recorded (step 4).

When the channels positions, e.g. the columns of pixels positions, are picked up, a third software, Processing, is used to create spatio-temporal diagram (step 5). The process consists in a loop over all the images of a video. For each image, the following steps are performed:

- The image is opened by the software,
- The chosen column of pixels corresponding to the channel of interest is copied,
- This column is incrementally pasted on the spatio-temporal diagram.

By pasting the same column of the successive images of the video, diagrams can be read from left to right to follow the chronology of events happening in the channel.

The same procedure is applied iteratively to each channel of the plate. At the end of the process, ten different spatio-temporal diagrams are obtained, one for each channel. The size of each diagram is ($\boldsymbol{m}$ *lines* x $\boldsymbol{k}$ *columns*) pixels. The X-axis of diagrams represents time whereas the Y-axis represents the position in the channels.

In *Figure 5*, one diagram created by the method described above is presented. It shows events occurring in the fifth channel from the left of the milli-structured plate. Several images extracted from the film at various time steps are presented above the diagram. In this case, the choice of the fifth channel is done on the best exposure conditions criterion. Except for both channels at the extremity of the plate (number 1 and 10), the same behavior is observed in the other channels of the milli-structured plate but it is not presented here for sake of concision.

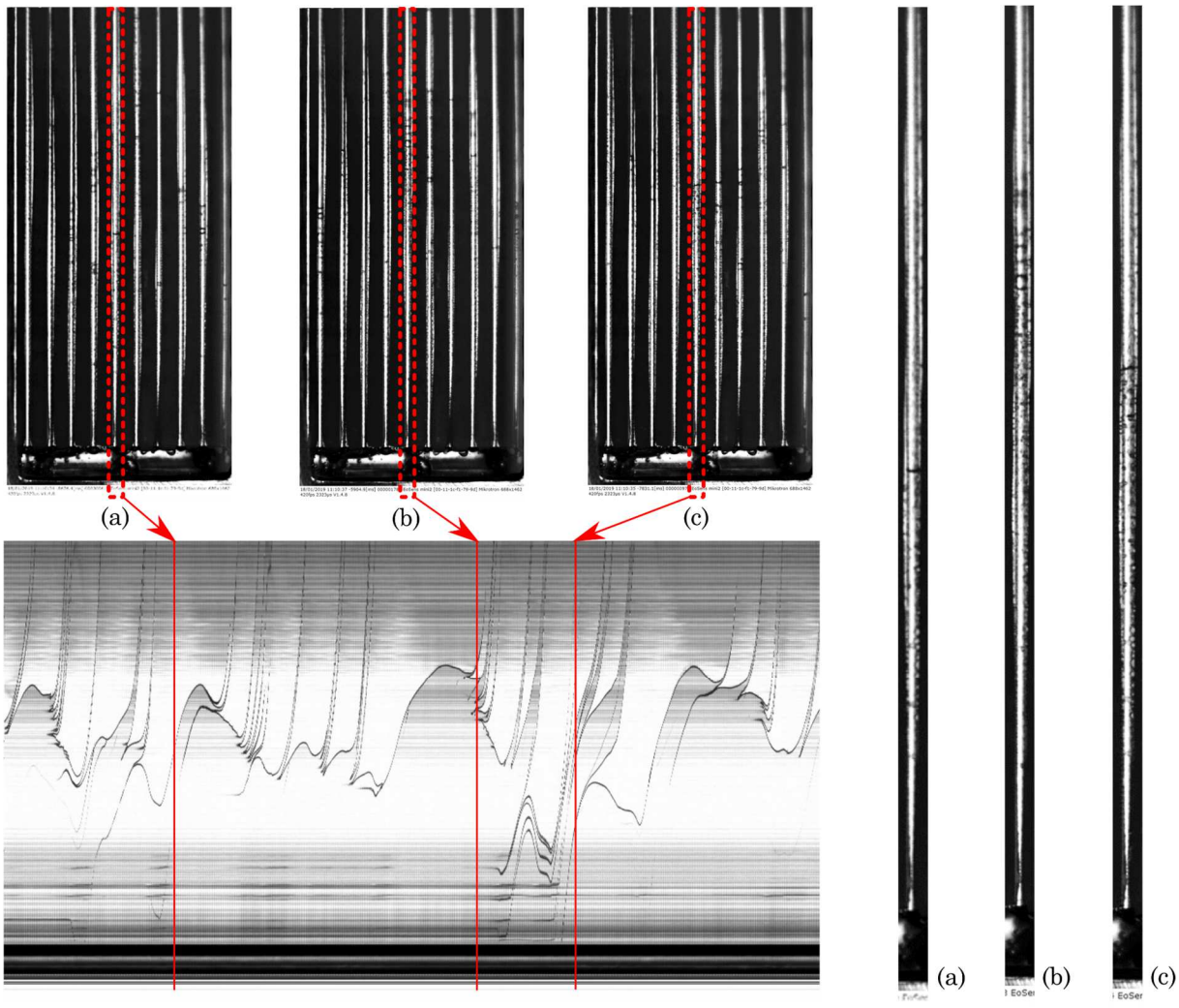

Figure 5: Full images of the 10-channels plate at three different moments (top left), zoomed-in views on the fifth channel at these same moments (right) while occurrence of the single-phase flow (a), the nucleation in cascade (b), the spontaneous nucleation (c) and the corresponding spatio-temporal diagram (bottom left) of the fifth channel; Oil flow rate 80

L/h, oil temperature 130°C, water flow rate 33 mL/min, water pre-heating temperature 50°C and atmospheric pressure.

In this experiment, the 10 diagrams corresponding to the 10 channels are composed of 4218 columns of pixels, with a height of 1746 pixels. It means that the original video was composed of 4218 images, and lasted approximately 10 seconds since the framerate chosen for recording was 420 fps.

This new method for the post-treatment of high-speed videos is not a silver bullet, it has some pros and cons that need to be discussed. On one hand, this innovative method enables the quick visualization of boiling phenomena over long durations (more than dozens of second if needed), it also enables a better understanding of the chronology and the causal links between phenomena. However, on the other hand, since the creation of these Spatio-Temporal Diagrams only focuses on one column of pixels extracted from the video, the diagram is not exhaustive. This issue can be tackled by calculating the average grey scale on the channel width, but both techniques are very sensitive to the video exposure conditions.

3.2. Dynamic vapor quality

The vapor quality is defined as the vapor mass fraction in the flow at the outlet of the test section:

$$x = \dot{m}_v/(\dot{m}_v + \dot{m}_l) \quad (1)$$

Where $\dot{m}_v$ denotes the mass flow rate of the vapor phase (kg/s) and $\dot{m}_l$ the mass flow rate of the liquid phase (kg/s).

When the heat is provided by an electrical cartridge, the specific flux can be considered uniform so that a local vapor quality can be assessed (Wang et al. [25], Lu et al. [16] and Sempértegui-Tapia et al. [9]). In this study, it is only possible to evaluate a global vapor

quality, i.e. the quality at the outlet of the test section, by writing the heat balance over the whole vaporizer:

$$\dot{Q}_{oil} = \dot{Q}_{water} + \dot{Q}_{loss} \quad (2)$$

Where $\dot{Q}_{oil}$ denotes the power transferred by the hot oil to the vaporizer (W), $\dot{Q}_{water}$ the received power by the water flow in the vaporizer (W) and $\dot{Q}_{loss}$ the heat losses of the vaporizer to the environment (W). The power transferred by the oil flow is defined by:

$$\dot{Q}_{oil} = \dot{m}_{oil}\, C_{p,oil}(T_{oil}^{in} - T_{oil}^{out}) \quad (3)$$

Where $\dot{m}_{oil}$ denotes the oil mass flow rate (kg/s), $C_{p,oil}$ the oil mass heat capacity (J/kg/K) and T_{oil}^{in} and T_{oil}^{out} the inlet and outlet oil temperatures in the vaporizer respectively (°C).

The power received by the water flow can be divided in two different terms, by differentiating the single-phase flow from the two-phase flow. A part of this power, $\dot{Q}_{sp}$, heats up the water to reach its boiling point:

$$\dot{Q}_{sp} = \dot{m}_w\, C_{p,w}(T_w^{eb} - T_w^{in}) \quad (4)$$

Where $\dot{m}_w$ denotes the mass flow rate of the water flow (kg/s), $C_{p,w}$ the water mass heat capacity (J/kg/K), T_w^{eb} the boiling temperature of water (°C) and T_w^{in} the inlet water temperature in the vaporizer (°C). For the particular case of the inlet water temperature in the vaporizer, the inlet water temperature is assumed equal to the temperature set in the pre-heating bath by neglecting heat losses along the pipe between the pre-heating bath and the vaporizer. The temperature probe measuring the water temperature in the distribution chamber is only used to estimate the temperature of the water flow entering the channels. The second part of the received power, $\dot{Q}_{tp}$, is dedicated to the partial vaporization of water:

$$\dot{Q}_{tp} = \dot{m}_w x \overline{\Delta H_v} \quad (5)$$

Where x denotes the global dynamic vapor quality and $\overline{\Delta H_v}$ the water mass latent heat of vaporization (J/kg). By substituting equations (3)-(4)-(5) in equation (2), the global vapor quality calculation becomes:

$$x = \left(\dot{m}_{oil}\, C_{p,oil}(T_{oil}^{in} - T_{oil}^{out}) - \dot{Q}_{losses} - \dot{m}_w Cp_w\left(T_w^{eb} - T_w^{in}\right)\right) / \left(\dot{m}_w \overline{\Delta H_v}\right) \qquad (6)$$

According to equation 6, the vapor quality value is closely related to heat losses. Heat losses can be assessed using an overall convective heat-transfer coefficient using the measured mean temperature of the plate (see Appendix A).

3.3. Uncertainty

The uncertainty presented in each plot in this study is calculated by the differential method, according to the following equation:

$$e^2_{F(P_1,\ldots,Pn)} = \sum_{i=1}^{n} \left(\frac{\partial F(P_1, \ldots, P_n)}{\partial P_i} e_{P_i} \right)^2 \qquad (7)$$

Where $F(P_1, \ldots, P_n)$ is the considered function of n parameters P_i, $e^2_{F(P_1,\ldots,Pn)}$ the estimated square error of the function and e_{P_i} the uncertainty of the parameter P_i.

All the temperature probes have an accuracy of ±0.15 °C. The oil flowmeter has an accuracy of ±0.1 kg/h, the water flowmeter of ±0.012 L/h and the tension measured in the heat flux meter of ±0.5 mV. The uncertainty of heat losses is estimated to 20% of the total value (cf. Appendix A). The estimation of the external surface of the test section is done by multiplying two measured dimensions. Since the insulation of the vaporizer is made of fabric, the measured dimension has an accuracy of ±1 cm because of the fabric looseness. The major source of uncertainty on the vapor quality is the temperature reading, more specifically the calculation of the difference of temperature in the heat balance, with typical relative uncertainties on the order of 35%.

3.4. Local vapor quality from local void fraction

Despite the lack of local data in the test section, a local void fraction can be determined using the spatio-temporal diagrams. The void fraction α is defined by:

$$\alpha = A_v/(A_v + A_l) \quad (8)$$

Where A_v (m²) and A_l (m²) are the cross-sectional areas occupied respectively by the vapor phase and the liquid phase.

A diagram allows the estimation of the local void fraction (at a given position in a channel) as a function of time. A time-averaged value is obtained by integrating over time:

$$\alpha_{av}(z) = 1/t_{tot} \int_0^{t_{tot}} \alpha(t,z)dt \quad (9)$$

Where $\alpha_{av}(z)$ is the mean local void fraction at position z, $\alpha(t,z)$ the local void fraction as a function of time at this position, and t_{tot} the total duration considered to calculate the mean value (s).

As shown in *Figure 6*, an ideal slug flow would produce alternating light and dark patches at a given location along the channel (corresponding to a given horizontal line of the diagram). The darker patches correspond to periods when the channel is full of liquid (liquid slug) and the lighter patches to the flow of vapor (bubble). According to the color of patches, the local void fraction, namely 0 when the channel is full of liquid and 1 when it is full of vapor, can be associated at each time to determine the function $\alpha_{av}(t,z)$.

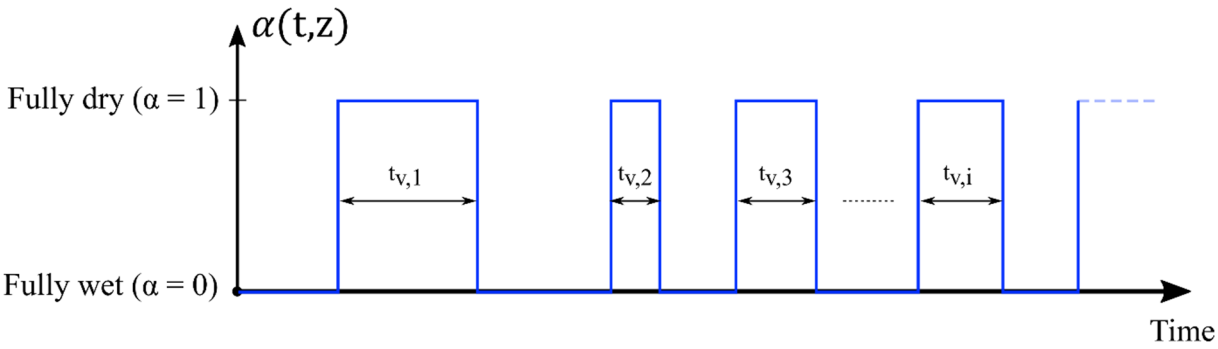

340

341 *Figure 6: Simplified evolution of the void fraction at a given position in a milli-channel under*

342 *slug flow conditions*

343 In other terms, at each moment in time, and for this location, the void fraction is equal either

344 to 0 or to 1 so that the mean void fraction over time can be computed as:

$$\alpha_{av}(z) = \sum_i t_{v,i}/t_{tot} \tag{10}$$

345 Where $t_{v,i}$ denotes the duration of a phase where the considered location is completely dry

346 (s). This ideal case is not so often encountered in the obtained diagrams. Some others patches

347 are visible with intermediary brightnesses and associated with local void fractions included

348 between 0 and 1. The calculation of the average void fraction of these patches is discussed in

349 the section 4.4.2.

350 Another quantity is required to estimate the local vapor quality: the slip ratio S_r (or velocity

351 ratio). This ratio compares the velocities of the liquid phase and the vapor phase and is

352 defined as:

$$S_r = v_v/v_l \tag{11}$$

353 Where v_v (m/s) and v_l (m/s) are the velocities respectively of the vapor phase and the liquid

354 phase. It exists various methods for the calculation of this ratio, in this work an indirect

355 method is used and detailed in section 4.4.2.

356 According to equation (1), the vapor quality can also be developed as:

$$x_{local} = v_v A_v \rho_v / (v_v A_v \rho_v + v_l A_l \rho_l) \quad (12)$$

Where ρ_v (kg/m^3) and ρ_l (kg/m^3) denote the densities respectively of the vapor phase and the liquid phase. By substituting equations (8) and (11) in equation (12), the calculation of the local quality becomes:

$$x_{local} = 1/(1 + (1 - \alpha)/\alpha * \rho_l/\rho_g * 1/S_r) \quad (13)$$

In this study, the mean void fraction over time and at a given position ($\alpha_{av}(z)$) is taken into account to estimate the local quality.

4. Results and Discussion

4.1. Diagrams interpretation

Some elementary patterns are observed in these complex diagrams such as brightness changes, multiple lines (curvy lines or straight horizontal lines). In *Figure 7*, a part of a diagram is zoomed in and some elements are explained.

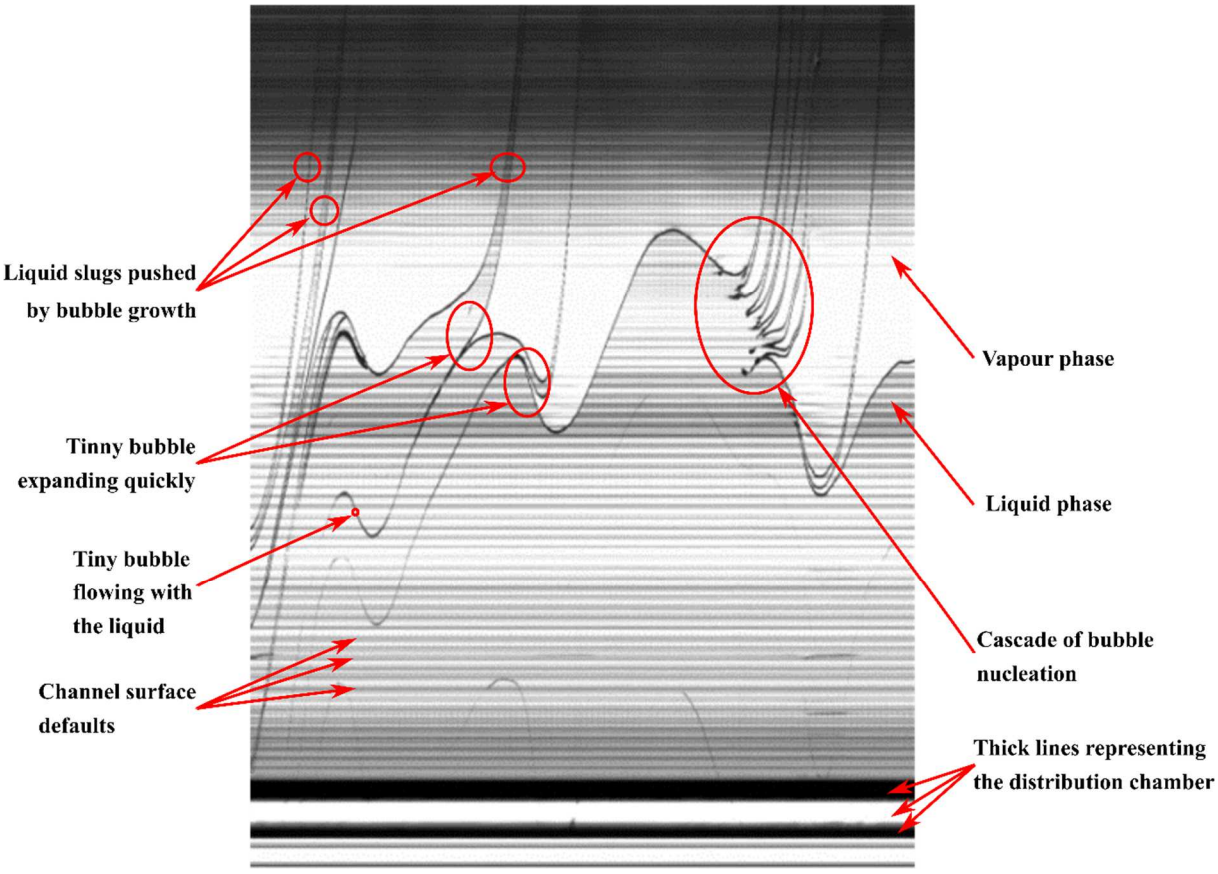

Figure 7: Focus on a spatio-temporal diagram part.

First invariant horizontal lines are visible over the entire diagram. Two cases can be distinguished: massive black and white lines at the bottom and other grey horizontal striae. Massive lines correspond to the "representation" of the distribution chamber whereas striae are caused by the channel surface machining defaults. Both these patterns are the direct result of the method used to create diagrams: since the same column of pixels is picked up from all images composing the film, invariant patterns caused by the geometry of the plate are reproduced in every column of the diagram.

Domains with various brightnesses are also visible in the diagrams, they represent either liquid or vapor phases of the boiling flow in the channel. Indeed, the brightness difference is related to light reflection either on the metal plate or through the liquid. The liquid and the produced vapor do not have the same behavior on the light path. Since the single-phase liquid

flow enters the channel at the bottom through the distribution chamber, darkest domains represent the liquid phase. Therefore, brightest domains represent the vapor phase. As a consequence, continuous black curves are the interfaces between phases:

- Black curves separating two domains with different exposures correspond to menisci between the liquid and vapor phases,
- Thin black curves in the darkest domain, e.g. the liquid phase, are tiny bubbles driven by the liquid and growing. These curves generally divide themselves into two lines: at this point, the bubble diameter is matching the cross section of the channel, leading to a fast expansion.

Numerous quasi-vertical filaments are observed in the upper side of the diagrams. A further observation shows two meniscuses at the upper and lower bounds of the dark domain composing these filaments. According the previous explanations, those filaments are the temporal visualization of a liquid slug expulsed by a bubble growth.

4.2. Hydrodynamics phenomena

In the presented diagrams, two main phenomena can be distinguished: a spontaneous nucleation (see *Figure 8 (a)*) and a periodic phenomenon (see *Figure 8 (b)*).

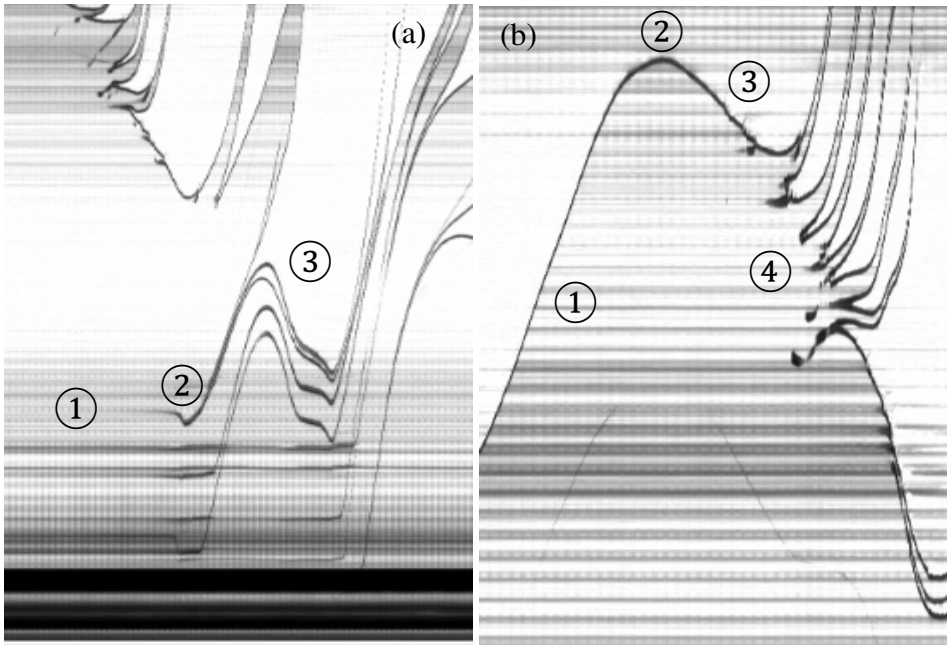

Figure 8: Focus on the diagram representation of the spontaneous nucleation (a) and the periodic phenomenon (b). (Oil flow rate 75 kg/h, oil temperature 130°C, water flow rate 2 L/h, water pre-heating temperature 130°C and atmospheric pressure).

Each phenomenon can be described step by step. For the spontaneous nucleation:

1. There is a sufficient amount of energy located on a nucleation site to enable the bubble nucleation. Bubble grows while remaining stuck on a channel wall.
2. The bubble grows until its size is sufficient to quit the nucleation site. Bubble take off is probably related to shear caused by the liquid up flow or down flow.
3. The bubble is driven by the liquid flow along the channel until it reaches a spot where it grows quickly. This fast size change induces reverse flow of the liquid upstream (below the bubble) and liquid slug ejection downstream (above the bubble).

For the periodic phenomenon:

1. The boiling activity of adjacent channels raises quickly the liquid level in the considered channel. The liquid then receives heat from the wall by convection.
2. The liquid level reaches a local maximum.

412 3. Events causing the previous level raise in other channels stop. The liquid level drops
413 meanwhile the liquid flow still receives heat from the wall.
414 4. The heat received by the liquid during these movements enables a chain nucleation
415 during the level drop. An average number of 5 or 6 strong bubble growths with
416 subsequent ejection of slugs is generally observed. The level of liquid, which naturally
417 drops, is further pushed down, accentuating the reverse flow observed.
418
419 *4.3. Global vapor quality*

420 *Figure 9* presents the influence of the water flow rate and the oil inlet temperature on the
421 global vapor quality. The quality of the vapor produced in the vaporizer decreases with the
422 water flow rate and increases with the oil inlet temperature. A total vaporization of the water
423 flow is observed when the oil inlet temperature is above 141°C.

424 This behavior is explained by the fact that heat transfer is limited on the oil side (this
425 assumption has been validated through additional experiments not detailed here for a sake of
426 brevity). For a given oil inlet temperature, the power provided by the oil to the test section is
427 independent of water flow rate. Considering that heat losses are roughly constant and
428 according to the heat balances (equations (2) and (4)), the higher the water flow rate, the
429 higher the power required for pre-heating. As a consequence, the vapor quality decreases with
430 the power available for vaporization.

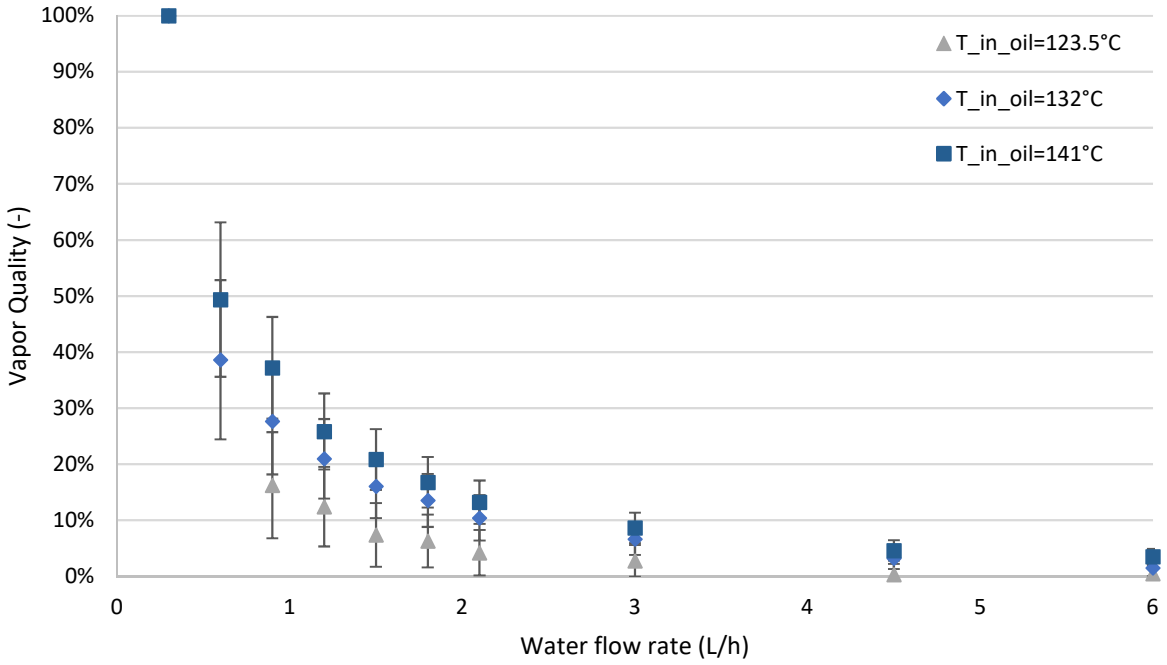

Figure 9: Influence of water flow rate and oil inlet temperature on vapor quality. (Oil flow rate 180kg/h, inlet water temperature 80°C and atmospheric pressure).

Additionally, considering that for a given water flow rate, and therefore a given pressure drop, the water boiling temperature remains the same, a higher oil inlet temperature leads to a higher exchanged power. Consequently, the available power for vaporization increases as well as the vapor quality.

4.4. Flow regimes and flow map

4.4.1. Flow regimes identification

As shown in *Figure 10*, four different flow regimes can be identified in the diagrams: the bubbly flow, the slug flow, the churn flow and the annular flow. It is important to notice that these regimes are not observed at the same time nor at the same position in the channel as the sketch in the top of *Figure 10* might suggest. Focusing the analysis on each flow regime observed, the bubbly flow regime (a) starts in the subcooled liquid flow, where the first bubbles nucleate. In the diagrams, these bubbles are spotted as thin black filaments in dark domains, and their movement follows the liquid flow. The slug flow (b) starts when the cross

section of a growing tiny bubble diameter meets the cross section of the channel. When that happens, the growth of the bubble accelerates, pushing down the liquid upstream and ejecting the liquid slug downstream. Depending on the inlet water flow rate, the slug can leave a trail, with more or less liquid. If the trail is significant, the churn flow (c) is observed on diagrams: it appears as a "turbulent" zone where slugs and projections are visible. Some small white spots are clearly visible and are a characteristic feature of this flow regime. On the contrary, if the liquid trail is thinner, the annular flow (d) is observed. On diagrams, bright sail shapes are visible on the right of every slug ejection patterns. The thin film of liquid evaporates with time until a new ejection of a slug happens.

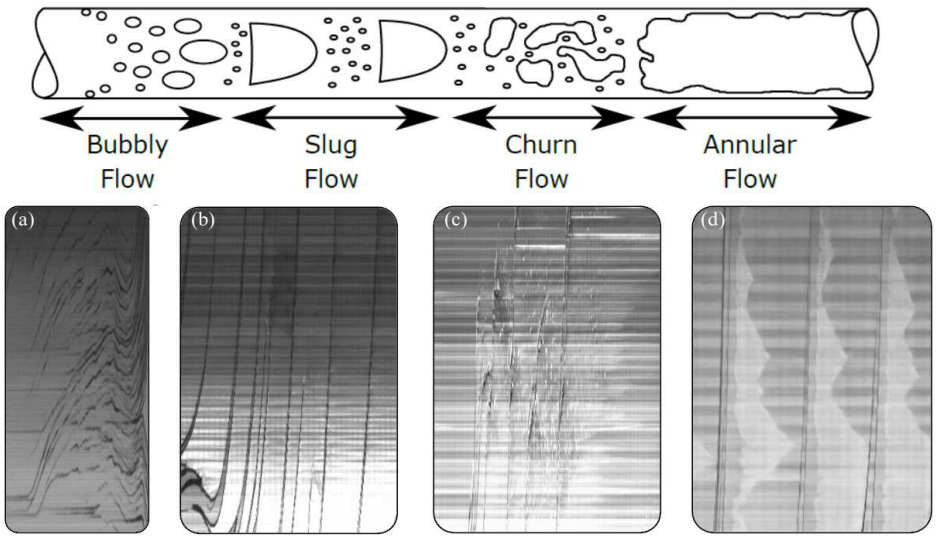

Figure 10: Flow regime identification in the Spatio-Temporal Diagrams: Bubbly flow (a), Slug flow (b), Churn flow (c) and Annular flow (d)

The next step of this work is repast these regimes on a map as a function of the liquid flow rate and the local vapor quality. Unfortunately, this latter feature is not measured directly: the next section demonstrates how the local quality can be estimated by a proper analysis of the diagrams.

4.4.2. Local vapor quality

4.4.2.1. *Estimation of the void fraction*

The first step in the determination of the local quality is to assess the mean void fraction over time thanks to spatio-temporal diagrams. *Figure 11* presents the local void fraction evolution according to patterns present on the diagram along a horizontal line corresponding to a strategic chosen position in the channel: below and above this position only bubbly flow or slug and annular flows are observed. On diagrams, these three flow regimes are associated with three patterns. Each pattern can be related to a value of the void fraction among:

- 0: only water is present in the channel.
- 1: only vapor is present in the channel.
- $0 < \alpha_{film} < 1$: since the film left by the ejected liquid slug is slowly vaporized, the mean value of the void fraction for the annual flow is not null. The default value was set at 0.5 awaiting validation.

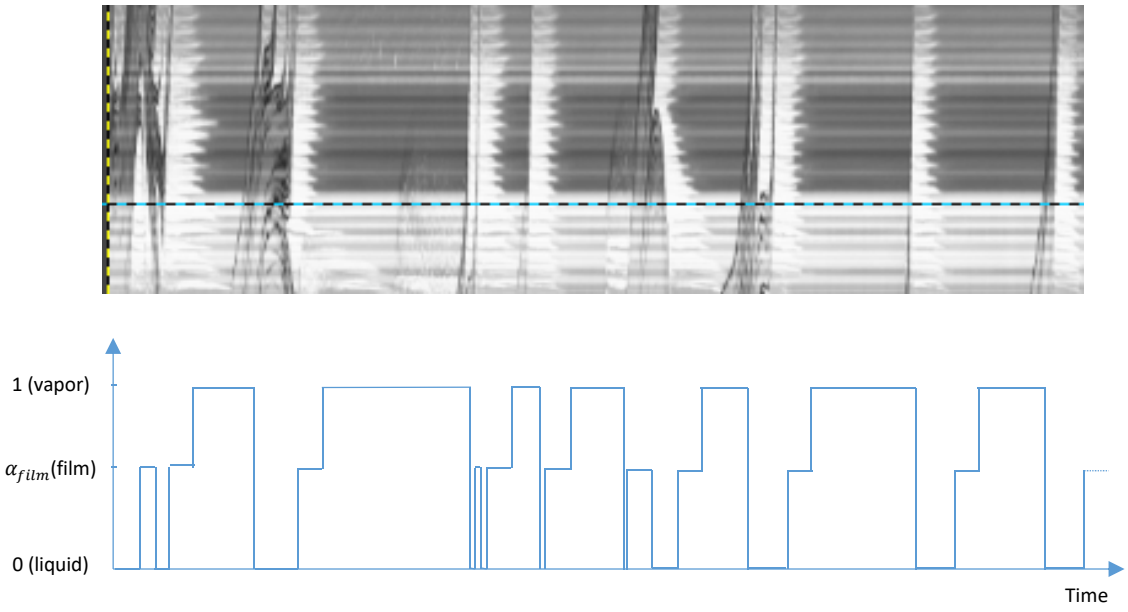

Figure 11: Evolution of the local void fraction along the limit defined between the bubbly flow and the slug flow. (Oil flow rate 180 kg/h, oil temperature 140°C, water flow rate 2 L/h, water pre-heating temperature 80°C and atmospheric pressure).

In *Figure 11* is presented an example of the method used to determine the value of the local void fraction from the analysis of a spatio-temporal diagram. Using equation (9) on the plot created in *Figure 11*, the mean value over time at the given position $\alpha_{av}(z)$ is calculated.

4.4.2.2. Estimation of the slip ratio

According to equation (13), the value of the slip ratio is needed for the calculation of the local quality from the local void fraction. Its value could be large enough to have a great influence on that calculation. In this study, the slip ratio is assumed constant, uniform and equal to a mean value in channels. This strong assumption is also used by some authors in the literature in models of void fraction using the local quality and a constant slip ratio. For instance, the Chen [26] model can be cited as a non-exhaustive example.

We set its value by comparing the global quality computed by the present method to the value inferred by heat balance (equation (6)). More precisely, an optimization on the slip ratio to reduce the quadratic error calculated by equation (14) is performed.

$$quadratic\ error = \sum_{i} \left(\left(x_{thermal,i} - x_{local,i} \right) / x_{thermal,i} \right)^2 \qquad (14)$$

Where $x_{thermal,i}$ and $x_{local,i}$ are respectively the global quality estimated through the heat balance and the local quality calculated by equation (13) at the channel outlet. The quadratic error is computed over the entire set of data for the following experimental conditions (index "i" represents each particular experiment): oil flow rate 180 kg/h, oil temperature 140°C, water flow rate [0.3 – 6] L/h, water pre-heating temperature 80°C and atmospheric pressure.

Figure 12 presents the optimized slip ratio calculated to fit properly the experimental data. In that particular case, the optimal value of S_r is equal to 60 for an assumed value of α_{film} of 0.5.

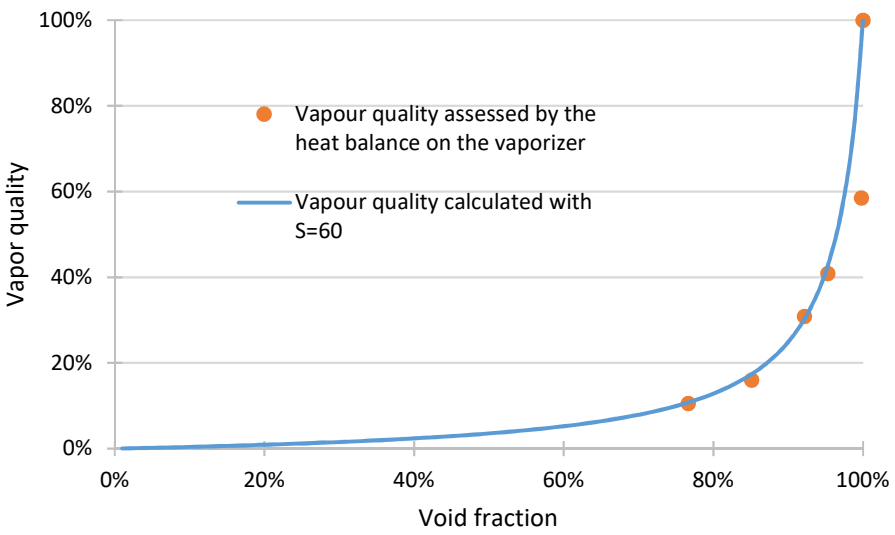

Figure 12: Optimized slip ratio for local quality assessment. (Oil flow rate 180 kg/h, oil temperature 140°C, water flow rate [0.3 – 6] L/h, water pre-heating temperature 80°C and atmospheric pressure).

4.4.2.3. Study of the relation between α_{film} and S_r

As alluded to, an assumption had to be made on the value of α_{film} to complete calculations in the previous section. The mean value of 0.5 was chosen since the film results from a liquid slug (void fraction = 1) and is finally totally vaporized (void fraction = 0). In this section, the effect of a change in the assumed value of α_{film} on the optimized value of S_r is discussed. First of all, a change in α_{film} affects the mean void fraction α_{av}. Using equation (9) on the plot of *Figure 12* leads to a simple calculation of α_{av} presented in equation (15) where the variation of $\alpha_{av}(z)$ with α_{film} is linear.

$$\alpha_{av}(z) = \frac{t_{vap}}{t_{tot}} + \frac{t_{film}}{t_{tot}} * \alpha_{film}, \begin{cases} t_{vap} = \sum_i t_{v,i} \\ t_{film} = t_{tot} - t_{vap} \end{cases} \quad (15)$$

Where t_{vap} and t_{film} are namely the duration of the vapor state and the duration of the film state (s) at position z and t_{tot} the total duration of the sequence considered for the integration (s).

The relation between S_r and α_{film} can be seen by using equation (13), introducing B_1 and B_2 respectively the constant ratios t_{film}/t_{tot} and t_{vap}/t_{tot} presented in equation (15):

$$S_r = x/(1-x) * (1/(B_1\alpha_{film} + B_2) - 1) * \rho_l/\rho_g \quad (16)$$

In particular, since the slip ratio is optimized by using the quality $x_{thermal}$ estimated by heat balance, the ratio $x_{thermal}/(1-x_{thermal})$ is independent of α_{film}. Equation (16) shows that there exists an infinity of couples $\{S_r; \alpha_{film}\}$ that can be a solution of this equality.

For a chosen value of α_{film}, the slip ratio used for the calculation of the local quality can have a significant influence on how the model fits the experimental data. However, for each value of α_{film}, an optimized slip ratio can be found to fit data, the remaining quadratic error is consistent for every couple $\{\alpha_{film};\ S_r^{optimized}\}$ put to the test. Therefore, the optimized slip ratio obtained for a chosen α_{film} can be considered as a relevant value. To go further, the optimized S_r is plotted as a function of the chosen α_{film} in *Figure 13*.

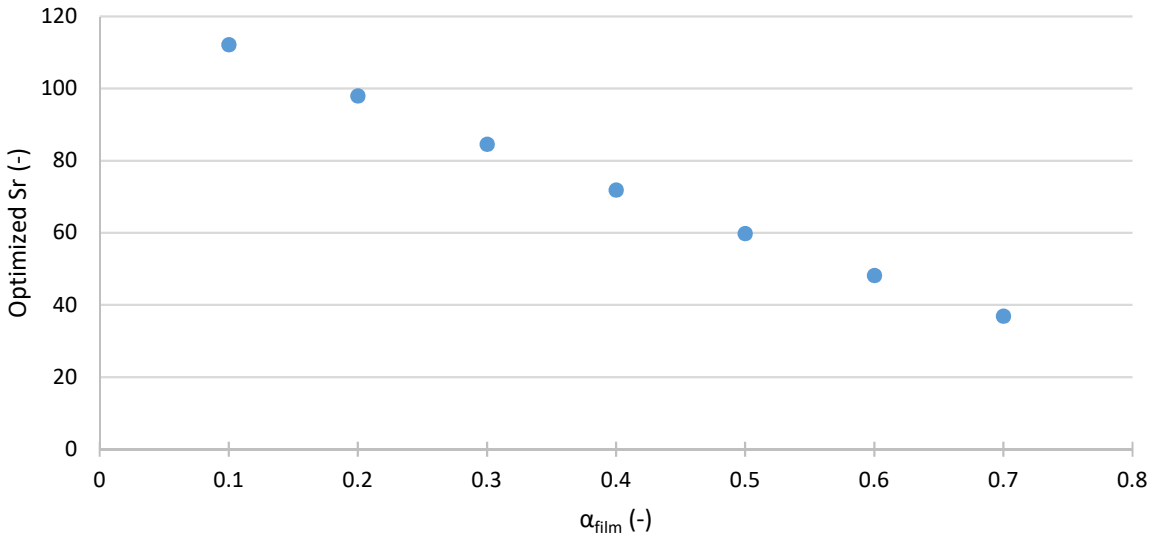

529

530 *Figure 13: Evolution of the optimized S_r with an increasing α_{film}*

531 The linear relation between the optimized S_r with an increasing α_{film} is at first sight
532 surprising. However, a closer look at equation (16) gives the explanation: since the magnitude
533 of variation of α_{film} is small, the function giving S can be assimilated to its asymptote for
534 this magnitude of variation.

535 The magnitude of optimized slip ratios is larger than the value calculated from models
536 available in the literature. The models determined by Zivi [27] or Smith [28] predict a slip
537 ratio depending on the vapor quality respectively up to 9.6 or 24.6. This difference of
538 magnitude can be explained by the reduction of the size of the flow. Ferret et al. [29]
539 attempted to measure experimentally slip ratios by image analysis. They found slip ratios
540 between 680 and 25 942, much higher than the predicted slip ratio using the Hewitt [30]
541 correlation between 3.6 and 9.5. Boiling water in 2 mm diameter vertical semi-circular
542 channels leads to a predominant slug flow regime causing liquid slug ejection and reverse
543 flow. These phenomena seem to lead towards higher mean slip ratios and this trend has to be
544 confirmed by additional works.

In conclusion, for the calculation of the average void fraction (equation (9)), there is no restriction on the value of α_{film} chosen, as long as its corresponding optimized slip ratio is used in the calculation of the local quality by equation (13). The local quality estimated thanks to this method can be used to draw the flow regimes maps developed in the next section.

4.4.3. Flow regimes map

Figure 14 presents the regimes map obtained by exploiting spatio-temporal diagrams extracted from the experiments.

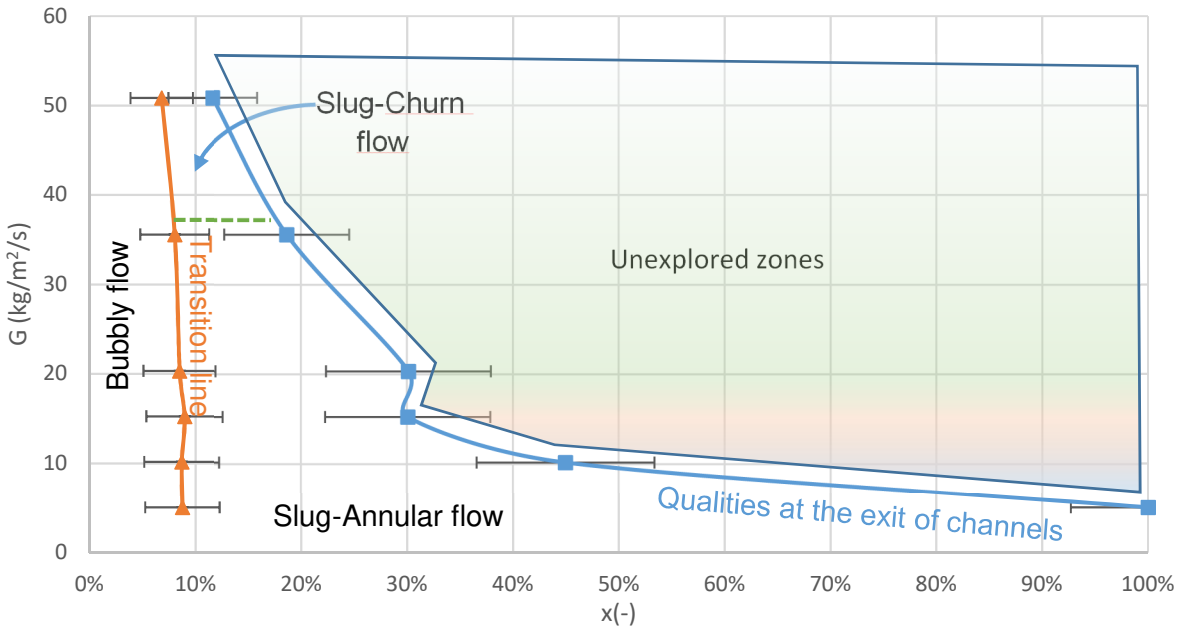

Figure 14: Flow regimes map (water flow rate [5 – 50.8] kg/m²/s, inlet water temperature 80°C, inlet oil temperature 132 °C, oil flow rate 179.3 kg/h.)

In this series of experiments, only one real transition line can be drawn between the bubble/slug flow and the slug/churn and annular flow. This transition occurs when the vapor quality reaches approximately 9%, which is consistent with Revellin and Thome [31] observation. In their work on the R-314a boiling flow, their flow regime map presents a

561 similar transition line for same specific flow rates but at a lower quality. There exists another
562 transition in the “slug” zone: above a specific flow rate of around 38 kg/m²/s, the churn flow
563 appears in the list of flow regimes visible in the diagrams among the annular and the slug
564 flow. Unfortunately, the transition line between bubbly flow and the mix of bubbly and slug
565 flow is not observed here as it can be seen in Revellin and Thome. Indeed the reverse flow is
566 so important in the channels that vapor pushes violently the liquid down to the distribution
567 chamber avoiding a permanent subcooled liquid flow at the entrance of channels. The
568 unexplored zone is due to the limitation of the test section on the vapor quality produced
569 inside the channels. Since the slug flow ejects a significant amount of liquid, the maximal
570 quality drops quickly by increasing the water flow rate.

571

572 **5. Conclusions**

573 Water flow boiling in ten milli-channels apparatus for steam production was experimentally
574 investigated in this work. The boiling phenomena were observed using a high-speed camera
575 to study flow patterns, flow regimes maps and vapor quality. The conclusions of the present
576 investigation are as follows:

577 • The innovative method using spatio-temporal diagrams is a useful tool for
578 understanding flow boiling inside milli-channels. It enables a quick overview of the
579 events occurring in channels and allows an estimation of local data such as the average
580 local void fraction at a given position in the channel.
581 • The boiling flow can be described by two main events: a spontaneous bubble
582 nucleation inside the liquid flow and a periodic oscillation inducing multiple
583 nucleation near the interface liquid/vapor.

584 - Every bubble created in channels induces a reverse flow and the ejection of a liquid
585 slug out of the channel. This phenomenon is a real issue for the improvement of the
586 vapor quality produced. Since the liquid is prematurely ejected from the channel by
587 the bubble growth, the transferred heat is not sufficient to ensure total vaporization.
588 - Flow regimes in channels were determined thanks to a parallel analysis of both spatio-
589 temporal diagrams and high-speed films. Four different regimes were identified:
590 bubbly, slug, churn and annular flows. Contrary to the case of a boiling flow in a
591 single channel, flow regimes are observed successively in the channel. The turnover of
592 flow regime is caused by the quick growth of bubbles in channels creating reverse
593 flow. It disturbs hydrodynamics in other channels via connected-vessel effect.
594 Nevertheless, a flow regime map can be drawn and it shows that the transition
595 between the bubbly flow and other flow regimes lies at 10% quality.
596 - The vapor quality produced in the vaporizer depends mostly on the water flow rate
597 and the inlet oil temperature. Total vaporization is possible in the vaporizer but at low
598 water flow rate.

599 For further understanding of flow boiling in small channels, new experiments are needed to
600 complete the exploration of the flow regime map presented in this work. The issue of liquid
601 slugs ejection caused by bubble growth also has to be tackled. To do that, new designs of
602 milli-channels with variable cross-sections should be designed in order to let the possibility
603 for the vapor to freely flow up to the outlet of the channels. Last but not least, the effect of
604 pressure on the boiling flow in such structure has to be studied through spatio-temporal
605 diagrams.

606 **6. Nomenclature**

A : Cross-sectional area (m²)

C_p : Mass calorific capacity (J/K/kg)

e : Uncertainty

F : Function (-)

$\overline{\Delta H_{vap}}$: Mass latent heat of vaporization (J/kg)

P : Parameter (-)

$\dot{m}$: Mass flow rate (kg/s)

n : index (-)

$\dot{Q}$: Power (W)

$\dot{q}$: Heat flux (W/m²)

S : Surface (m²)

S_r : Slip ratio (-)

t : Time (s)

T : Temperature (°C)

v : Phase velocity (m/s)

x : Vapor quality (-)

Greek symbols

α : Void fraction (-)

ρ : Density (kg/m^3)

Subscripts

$film$: Liquid film

l : Liquid phase

$local$: Calculated locally

oil : Oil flow

sp : Single-phase

$thermal$: Calculated via the heat balance

tot : Total

tp : Two-phase

v/vap : Vapor phase

w : Wall

$water$: Water flow

Superscripts

eb : Boiling point

in : Inlet

out : Outlet

7. Acknowledgments

Authors acknowledge BPI France for their financial support of the FAIR Project ("Fabrication Additive pour l'Intensification des Réacteurs"; n°2015-PRSP-16), in the frame of the "Programme d'investissements d'avenir", and the ENERBATIN Project supported by Région Grand-Est through CPER 2015-2020. In addition, authors acknowledge the mechanical workshop and the electronic service (SIEL) of the Reactions and Chemical Engineering Laboratory in Nancy for their precious help during the construction and the instrumentation of the test bench and the test section.

8. References

[1] A. Stankiewicz, J.A. Moulijn, Re-Engineering the Chemical Processing Plant: Process Intensification, CRC Press, 2003.

[2] T.R. Dietrich, ed., Microchemical Engineering in Practice, WILEY, 2009.

[3] V. Hessel, A. Renken, J.C. Schouten, J. Yoshida, Micro Process Engineering, 2009.

[4] K. Surla, Hydrogène, Tech. l'ingénieur. TIB319DUO. (2019). https://www.techniques-ingenieur.fr/base-documentaire/procedes-chimie-bio-agro-th2/fabrication-des-grands-produits-industriels-en-chimie-et-petrochimie-42319210/hydrogene-j6368/.

[5] F. Giroudière, A. Le Gall, Production des gaz de synthèse, Tech. l'Ingénieur. TIB329DUO. (2012). https://www.techniques-ingenieur.fr/base-documentaire/procedes-chimie-bio-agro-th2/procedes-industriels-de-base-en-chimie-et-petrochimie-42329210/production-des-gaz-de-synthese-par-vaporeformage-j5480/.

[6] J. Frauhammer, G. Eigenberger, L. V. Hippel, D. Arntz, A new reactor concept for endothermic high-temperature reactions, Chem. Eng. Sci. 54 (1999) 3661–3670. doi:10.1016/S0009-2509(98)00454-0.

[7] J. Bhat, Shrikant A.; Sadhukhan, Process Intensification Aspects for Steam Methane Reforming: An Overview, Am. Inst. Chem. Eng. AIChE J. 55 (2009) 408–422. doi:10.1002/aic.11687.

[8] V. Solotych, D. Lee, J. Kim, R.L. Amalfi, J.R. Thome, Boiling heat transfer and two-phase pressure drops within compact plate heat exchangers: Experiments and flow visualizations, Int. J. Heat Mass Transf. 94 (2016) 239–253. doi:10.1016/j.ijheatmasstransfer.2015.11.037.

[9] F.D. Sempértegui-Tapia, G. Ribatski, Flow boiling heat transfer of R134a and low GWP refrigerants in a horizontal micro-scale channel, Int. J. Heat Mass Transf. 109 (2017) 938–948. doi:10.1016/j.ijheatmasstransfer.2017.02.066.

[10] G.M. Lazarek, S.H. Black, Evaporative heat transfer, pressure drop and critical heat flux in a small vertical tube with R-113, Int. J. Heat Mass Transf. 25 (1982) 945–960. doi:10.1016/0017-9310(82)90070-9.

[11] P.A. Kew, K. Cornwell, CORRELATIONS FOR THE PREDICTION OF BOILING HEAT TRANSFER IN SMALL-DIAMETER CHANNELS, Appl. Therm. Eng. 17 (1997) 705–715.

[12] A.S. Pamitran, K. Il Choi, J.T. Oh, H.K. Oh, Forced convective boiling heat transfer of R-410A in horizontal minichannels, Int. J. Refrig. 30 (2007) 155–165. doi:10.1016/j.ijrefrig.2006.06.005.

[13] L. Cheng, G. Xia, Fundamental issues, mechanisms and models of flow boiling heat transfer in microscale channels, Int. J. Heat Mass Transf. 108 (2017) 97–127. doi:10.1016/j.ijheatmasstransfer.2016.12.003.

[14] X. Fang, Y. Yuan, A. Xu, L. Tian, Q. Wu, Review of correlations for subcooled flow boiling heat transfer and assessment of their applicability to water, Fusion Eng. Des. 122 (2017) 52–63. doi:10.1016/j.fusengdes.2017.09.008.

[15] L. Yin, R. Xu, P. Jiang, H. Cai, L. Jia, Subcooled flow boiling of water in a large aspect ratio microchannel, Int. J. Heat Mass Transf. 112 (2017) 1081–1089. doi:10.1016/j.ijheatmasstransfer.2017.05.028.

[16] Q. Lu, D. Chen, C. Li, X. He, Experimental investigation on flow boiling heat transfer in conventional and mini vertical channels, Int. J. Heat Mass Transf. 107 (2017) 225–243. doi:10.1016/j.ijheatmasstransfer.2016.11.020.

[17] S.M. Kim, I. Mudawar, Review of databases and predictive methods for heat transfer in condensing and boiling mini/micro-channel flows, Int. J. Heat Mass Transf. 77 (2014) 627–652. doi:10.1016/j.ijheatmasstransfer.2014.05.036.

[18] J.C. Chen, Correlation for boiling heat transfer to saturated fluids in convective flow, Ind. Eng. Chem. Process Des. Dev. 5 (1966) 322–329. doi:10.1021/i260019a023.

[19] J. Yan, Q. Bi, Z. Liu, G. Zhu, L. Cai, Subcooled flow boiling heat transfer of water in a circular tube under high heat fluxes and high mass fluxes, Fusion Eng. Des. 100 (2015) 406–418. doi:10.1016/j.fusengdes.2015.07.007.

[20] S.G. Kandlikar, Fundamental issues related to flow boiling in minichannels and microchannels, Exp. Therm. Fluid Sci. 26 (2002) 389–407. doi:10.1016/S0894-1777(02)00150-4.

[21] J.R. Thome, State-of-the-art overview of boiling and two-phase flows in microchannels, Heat Transf. Eng. 27 (2006) 4–19. doi:10.1080/01457630600845481.

[22] V. Kumar, Vikash, K.D.P. Nigam, Multiphase fluid flow and heat transfer characteristics in microchannels, Chem. Eng. Sci. 169 (2017) 34–66. doi:10.1016/j.ces.2017.01.018.

[23] L. Chen, Y.S. Tian, T.G. Karayiannis, The effect of tube diameter on vertical two-phase flow regimes in small tubes, Int. J. Heat Mass Transf. 49 (2006) 4220–4230. doi:10.1016/j.ijheatmasstransfer.2006.03.025.

[24] M.E. Steinke, S.G. Kandlikar, An Experimental Investigation of Flow Boiling Characteristics of Water in Parallel Microchannels, J. Heat Transfer. 126 (2004) 518.

683 doi:10.1115/1.1778187.
684 [25] S. Wang, X. Bi, S. Wang, Boiling heat transfer in small rectangular channels at low
685 Reynolds number and mass flux, Exp. Therm. Fluid Sci. 77 (2016) 234–245.
686 doi:10.1016/j.expthermflusci.2016.04.022.
687 [26] J.J.J. Chen, A further examination of void fraction in annular two-phase flow, Int. J.
688 Heat Mass Transf. 29 (1986) 1760–1763. doi:10.1016/0017-9310(86)90116-X.
689 [27] S.M. Zivi, Estimation of steady state steam void fraction by means of the principle of
690 minimum entropy production, Trans. ASME, J. Heat Transf. 86 (1964) 247–252.
691 [28] S.L. Smith, Void fractions in two- phase flow. A correlation based upon an equal
692 velocity head model, 18 (1969) 647–664. doi:10.1243/pime_proc_1969_184_051_02.
693 [29] C. Ferret, L. Falk, U. D'Ortona, A. Chenu, T.T. Veenstra, Introduction of image
694 analysis for the quantification of the boiling flow heat transfer, Chem. Eng. J. 101
695 (2004) 357–365. doi:10.1016/j.cej.2003.10.028.
696 [30] G. Hetsroni, G.F. Hewitt, Void Fraction, in: M. Graw-Hill (Ed.), Handb. Multiph. Syst.
697 Chapter 2.3., New York, 1982. doi:10.1615/AtoZ.v.void_fraction.
698 [31] R. Revellin, J.R. Thome, A new type of diabatic flow pattern map for boiling heat
699 transfer in microchannels, J. Micromechanics Microengineering. 17 (2007) 788–796.
700 doi:10.1088/0960-1317/17/4/016.
701

Appendix A: Heat losses experiments

This section develops the methodology adopted for the estimation of the convective heat-transfer coefficient presented in this work for the assessment of heat losses. Two series of experiments were carried out on the test bench in order to estimate this coefficient: one by using heat-flux meters and a second one by exploiting cooling kinetics of the test section.

1. Heat losses measured by heat-flux meter

Since one of the heat flux meters is glued on the glass window, it prevents visualizing phenomena in the test section. As the present work is focused on the visualization and the characterization of the flow regimes and their influence on the vapor quality, it has been chosen to assess heat losses by using an overall convective heat-transfer coefficient at the external surface of the vaporizer. For this campaign, only an oil flow is used to provide heat to the test section. The experimental operating conditions used are gathered in *Table 1*:

Parameter	Range	Unity
Oil flow rate	46 – 157	kg/h
Inlet Oil temperature	38.8 - 147	°C

Table A.1 Ranges of operating conditions used for the heast losses measurment by heat-flux meters

The heat flux of both sensors are picked up and heat losses are calculated by:

$$\dot{Q}_{losses} = \dot{q}_{window} S_{window} + \dot{q}_{insulator} S_{insulator} \quad \text{(A.1)}$$

Where $\dot{q}$ denotes the heat flux of the considered surface (W/m²), and S its area (m²).'

The raw results are presented in *Figure A.1*; uncertainties are estimated by equation (7). Since the external area of the test section is known (0.11 m²), the heat-transfer coefficient can be

estimated by dividing the slope by the external area. The convective heat-transfer coefficient calculated by this way is equal to 13.5 W/m²/K

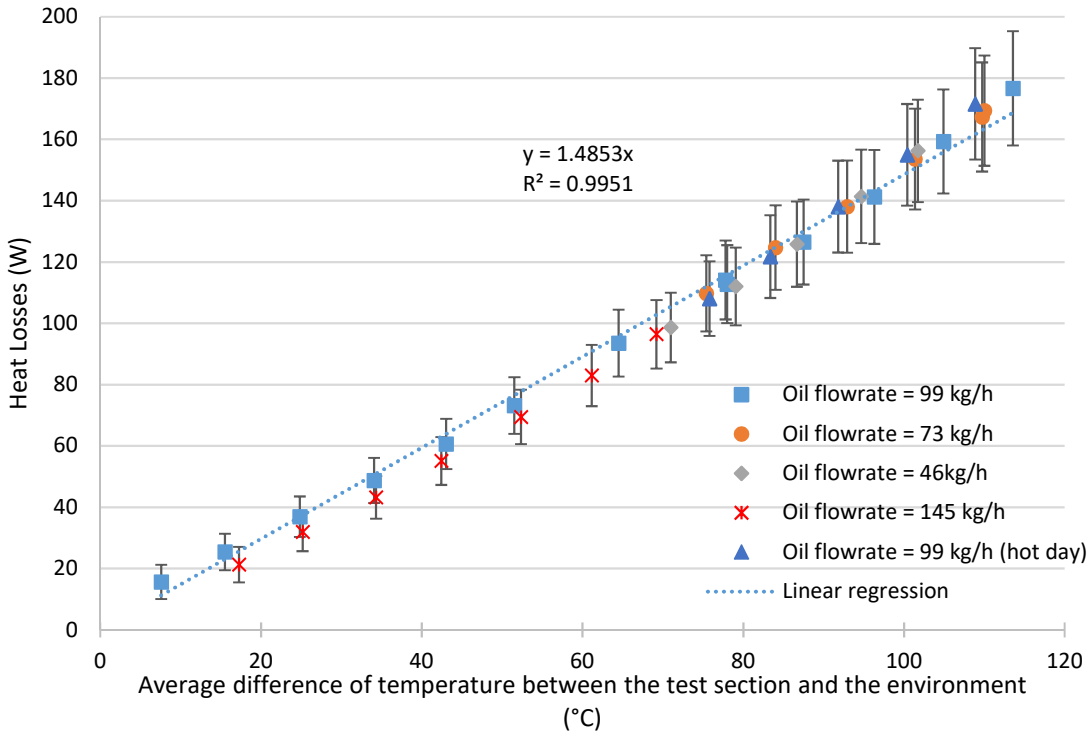

Figure A.1: Heat losses measured on the test bench by heat-flux meters.

2. *Heat-transfer coefficient estimated from the cooling kinetics of the test bench*

For this campaign, the oil and the water flow temperatures are set on the same value to speed up the heating of the test section. When all temperatures of the test section are stabilized, the circulation of both fluids is stopped. Then, temperatures are picked up every 2 seconds until the ambient temperature is reached. The initial temperatures tested are: {62.8; 72; 80.8; 98.7; 107.9} °C. Since there are 6 temperatures picked in the milli-structured plate, the decreasing mean value of these temperatures as a function of time is considered. An example of this evolution is plotted in *Figure A.2*.

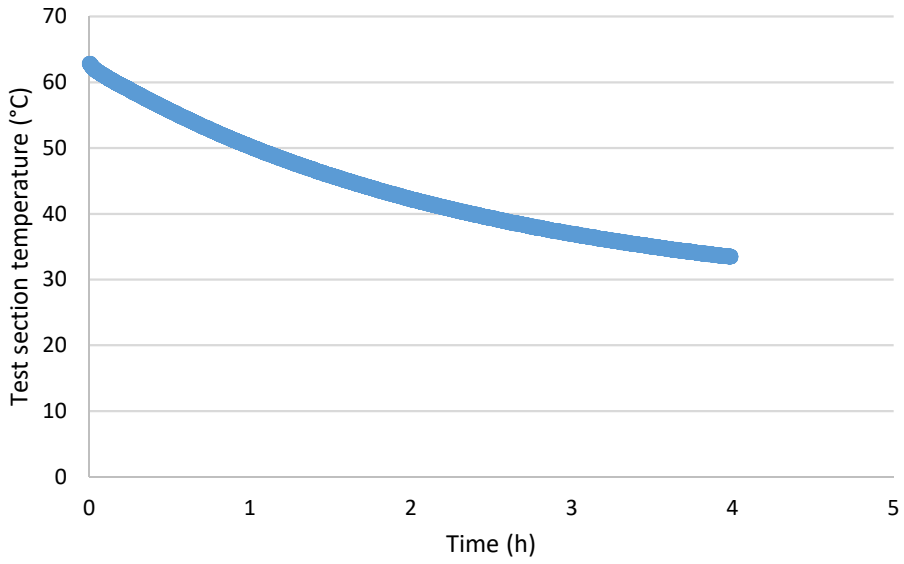

Figure A.2: Cooling kinetics of the test section from an initial temperature of 62.8°C

The pick-up process is in fact stopped before the end of the cooling. Only the initial slope is considered for the estimation of the convective heat-transfer coefficient. A heat balance on the test section during the cooling process gives:

$$dT/dt = -h_{loss}S/(m_{test\ section}C_{p\ test\ section}) * (T - T_{environment}) \quad \text{(A.2)}$$

Where h_{loss} (W/m²/K) is the convective heat-transfer coefficient.

Thanks to the external area, the mass and the heat capacity of the test section, the initial difference of temperature between the test section and the environment and the initial slope of the curve, the heat-transfer coefficient can be calculated. The results are consigned in *Figure A.3*.

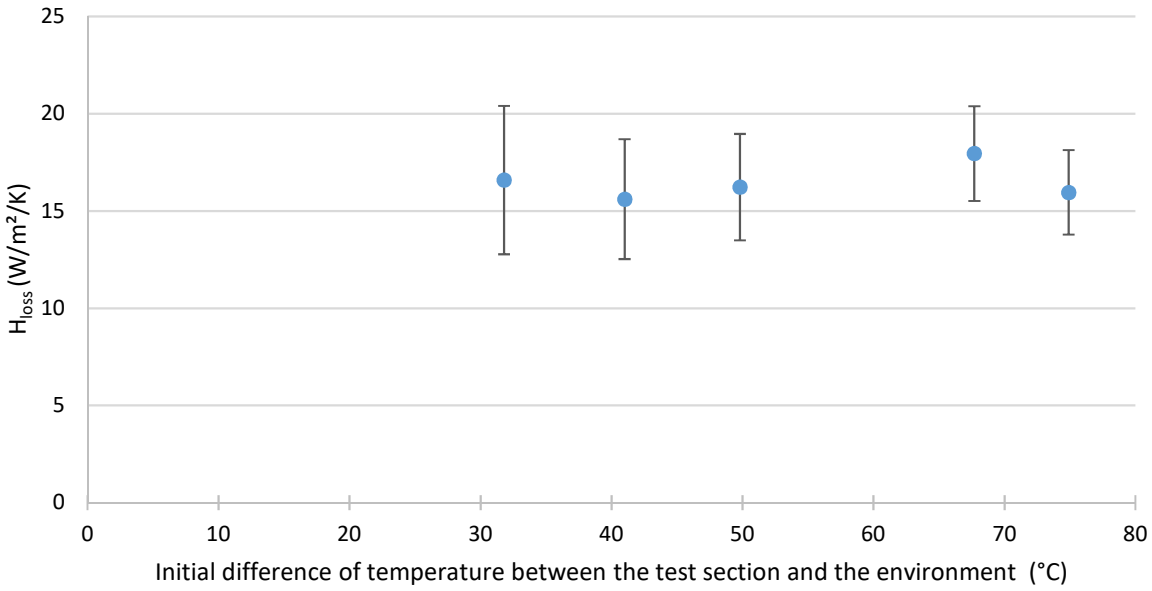

742

743 *Figure A.3: Convective heat-transfer coefficient calculated from the cooling kinetics of the*

744 *test section.*

745 According to uncertainty of measurements, both methods lead to close results, it has been

746 decided that the convective heat-transfer coefficient is set to 15 W/m²/K considering an

747 uncertainty of 20% of the calculated value.

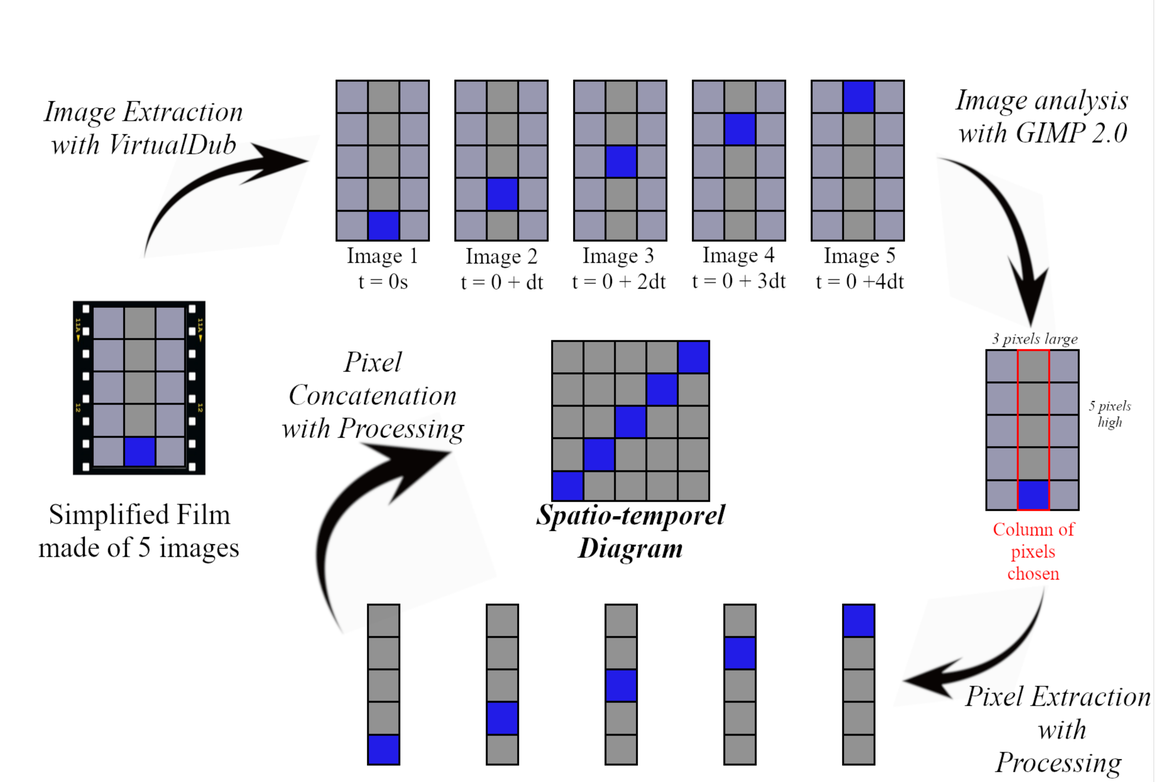
Image Extraction with VirtualDub
Image 1 t = 0s
Image 2 t = 0 + dt
Image 3 t = 0 + 2dt
Image 4 t = 0 + 3dt
Image 5 t = 0 +4dt
Image analysis with GIMP 2.0
3 pixels large
5 pixels high
Column of pixels chosen
Pixel Extraction with Processing
Pixel Concatenation with Processing
Spatio-temporel Diagram
Simplified Film made of 5 images

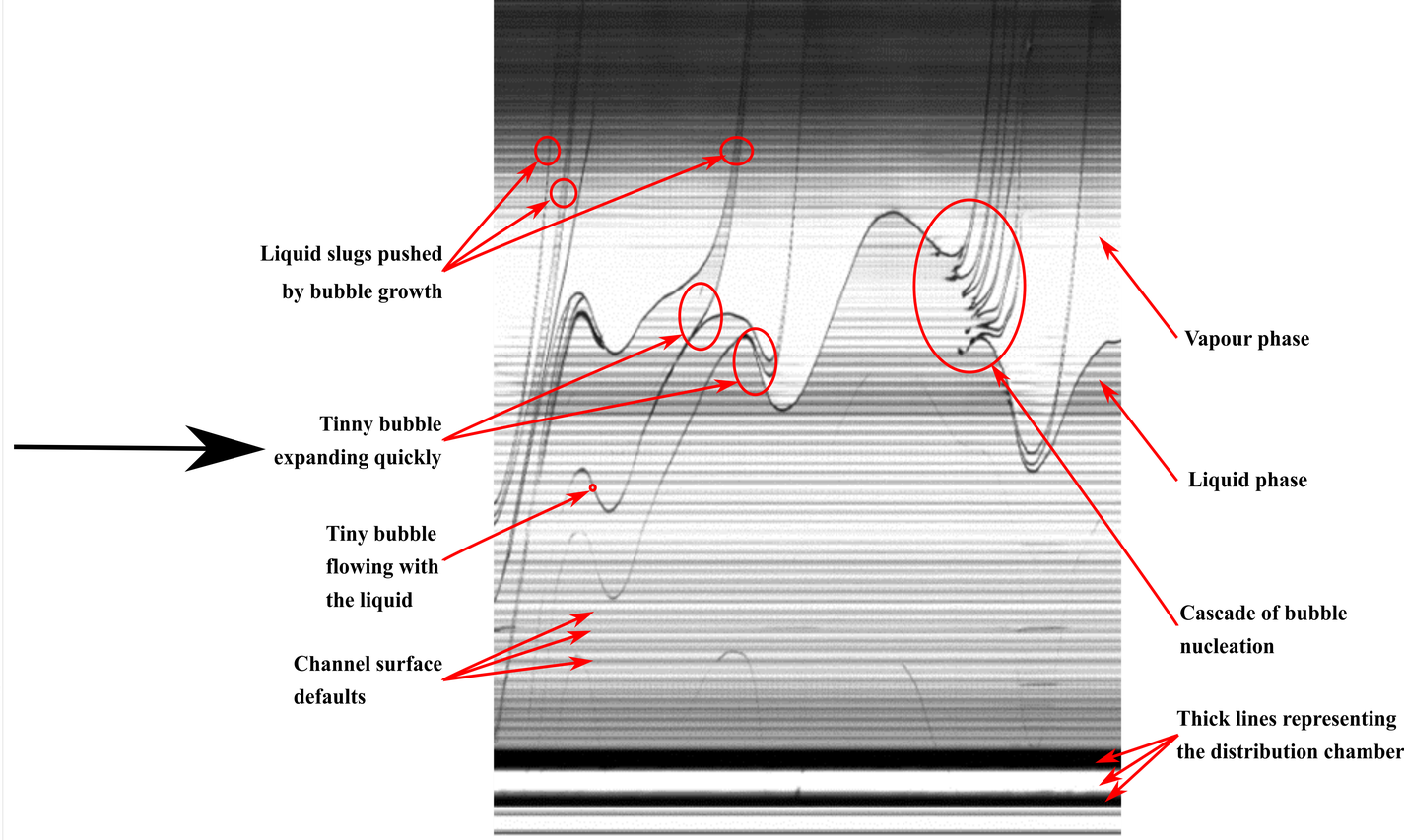
Liquid slugs pushed by bubble growth
Tinny bubble expanding quickly
Tiny bubble flowing with the liquid
Channel surface defaults
Vapour phase
Liquid phase
Cascade of bubble nucleation
Thick lines representing the distribution chamber